EVIDENT | OLYMPUS

THESE ARE NOT FIREWORKS

This is a single colony of Gloeotrichia captured using a 10X X Line objective.

IMAGE: © HAKAN KVARNSTROM

See the truth with X Line™ objectives.

Scan the code to discover more.

X LINE

Contact your local sales representative or visit **olympus-lifescience.com/this-is-xline** to learn more.

Journal of Microscopy

Journal of Microscopy, Vol. 267, Issue 2 2017, pp. 160–175 doi: 10.1111/jmi.12556
Received 9 August 2016; accepted 21 February 2017

A protocol for registration and correction of multicolour STED superresolution images

E. HEBISCH*, E. WAGNER†,‡, V. WESTPHAL*, J.J. SIEBER§ & S.E. LEHNART†,‡
**Department of NanoBiophotonics, Max Planck Institute for Biophysical Chemistry, Göttingen, Germany*
†Heart Research Center Göttingen, Department of Cardiology & Pulmonology, University Medical Center Göttingen, Göttingen, Germany
‡German Center for Cardiovascular Research (DZHK) site Göttingen, Göttingen, Germany
§Leica Microsystems CMS GmbH, Mannheim, Germany

Key words. Image registration, multicolour imaging, ryanodine receptor, STED microscopy, targeted superresolution microscopy.

Summary

Multicolour fluorescence imaging by STimulated Emission Depletion (STED) superresolution microscopy with doughnut-shaped STED laser beams based on different wavelengths for each colour channel requires precise image registration. This is especially important when STED imaging is used for co-localisation studies of two or more native proteins in biological specimens to analyse nanometric subcellular spatial arrangements. We developed a robust postprocessing image registration protocol, with the aim to verify and ultimately optimise multicolour STED image quality. Importantly, this protocol will support any subsequent quantitative localisation analysis at nanometric scales. Henceforth, using an approach that registers each colour channel present during STED imaging individually, this protocol reliably corrects for optical aberrations and inadvertent sample drift. To achieve the latter goal, the protocol combines the experimental sample information, from corresponding STED and confocal images using the same optical beam path and setup, with that of an independent calibration sample. As a result, image registration is based on a strategy that maximises the cross-correlation between sequentially acquired images of the experimental sample, which are strategically combined by the protocol. We demonstrate the general applicability of the image registration protocol by co-staining of the ryanodine receptor calcium release channel in primary mouse cardiomyocytes. To validate this new approach, we identify user-friendly criteria, which – if fulfilled – support optimal image registration. In summary, we introduce a new method for image registration and rationally based postprocessing steps through a highly standardised protocol for multicolour STED imaging, which directly supports the reproducibility of protein co-localisation analyses. Although the reference protocol is discussed exemplarily for two-colour STED imaging, it can be readily expanded to three or more colours and STED channels.

Correspondence to: Stephan E. Lehnart, Heart Research Center Göttingen, Department of Cardiology & Pulmonology, University Medical Center Göttingen, Robert-Koch-Str. 40, 37075 Göttingen, Germany. Tel: +49 551 39 10575; Fax: +49 551 39 10650; e-mail: slehnart@med.uni-goettingen.de

Introduction

Stimulated emission depletion (STED) microscopy provides subdiffraction resolution in far-field fluorescence microscopy, which increases the accuracy of fluorescence imaging and localisation of complex biological samples (cf. Berning *et al.*, 2012; Chojnacki *et al.*, 2012; Wagner *et al.*, 2012; D'Este *et al.*, 2015; Brandenburg *et al.*, 2016), just to name a few). As a consequence of improved resolution at nanometric scales, fluorescence image processing and image analysis procedures need to be adjusted and refined, especially to quantitatively assess frequent co-localisation and/or other specific nanoscale arrangements between two or more proteins in cells (Zinchuk *et al.*, 2007; Buckers *et al.*, 2011; Dunn *et al.*, 2011). Notably, conventional multicolour confocal microscopy is limited by diffraction-induced blurring that generally leads to overestimation of the actual signal overlap if two or more dye-labelled objects are densely distributed, and thus of the true extent of protein co-localisation in multicolour images. In contrast, STED provides a resolution down to 20–30 nm in cells (Donnert *et al.*, 2006; Gottfert *et al.*, 2013; Danzl *et al.*, 2016). Although the improved nanoscale resolution is achieved directly, that is, without any image postprocessing, significantly reducing image regions of potentially erroneous signal overlap, it may also inadvertently amplify artefacts due to sample drift or optical aberrations. Hence, to explicitly address and rationally limit such artefactual image information, that is, due to drift or aberration, multicolour STED imaging – cf. (Neumann *et al.*, 2010; Opazo *et al.*, 2010; Chen *et al.*, 2013; Westin *et al.*, 2014) – requires a robust and precise evaluation strategy to allow for reliable quantitative analyses.

In STED microscopy, the excitation beam is usually superimposed with a second, red-shifted laser beam (the STED beam) with a central intensity minimum. This minimum (surrounded by the doughnut-shaped maximum of the STED depletion beam) defines where the detectable fluorescence signals localise by switching off any peripheral fluorescent molecules (Hell, 2007; Hell, 2015; Hell & Wichmann, 1994). Therefore, if a single STED laser is used for line- or pixel-interleaved multicolour STED imaging, image registration – in contrast to other superresolution approaches – is not necessary, because scanning with one STED laser is sufficient to target two spectrally distinct fluorophores simultaneously, effectively generating a one-pass multicolour image (Buckers *et al.*, 2011; Bethge *et al.*, 2013; D'Este *et al.*, 2016).

For general STED applicability, however, in particular multicolour sample imaging, additional STED laser beams are required, dyes with appropriately matching photochemical properties and/or a number of different fluorescent dyes, that can be applied in a given sample (Donnert *et al.*, 2007; Meyer *et al.*, 2008; Blom *et al.*, 2012). Consequently, whenever two or more STED lasers are used, images of different colours and corresponding channels are acquired through sequential frame scanning. This is necessary to avoid inadvertent overlap between the excitation and emission bands in the context of multiple fluorescent dyes present in the sample, and also to avoid potentially disadvantageous overlap between a dye's emission or excitation band and the STED laser wavelength, which is needed to deplete the other dye(s) in the same spot to achieve nanoscale resolution. Sequential scanning thus minimises potential artefacts due to cross-talk between two or more colour channels. However, this comes at the cost of more complex setups for STED microscopy as well as corresponding image acquisition schemes, which introduce additional factors and sources for errors, which can increase the potential for mismatch between images of individual colour channels.

Taken together, three reasons for image registration mismatch appear prevalent: (1) inadvertent displacement between laser beams in a given experimental setup, either between the excitation and STED laser beams, between the different excitation laser beams or – most important for multicolour protocols – between the different STED laser beams; (2) chromatic aberrations and (3) inadvertent drift or movement, both lateral or axial, of the biological sample between consecutive imaging scans. Typically, these three issues cannot be addressed separately during imaging, but rather occur in combination and can lead to a highly undesirable offset between the different colour channels. Therefore, for reliable and quantifiable image analysis based on fluorescence signals overlaid from two or more different colour channels, a rational, rigorous and user-friendly strategy is needed.

Here, we present a concise approach for the correction of any registration mismatch between multicolour STED images that are sequentially obtained using two separate STED beams. By defining a step-wise protocol based on rational criteria, we show how STED images can be corrected for all three prevalent causes of registration mismatch. Thereby, colour-aligned high-quality STED images are effectively prepared and if necessary corrected prior to quantitative co-localisation analysis. Additionally, we provide a custom-written protocol for MATLAB that executes the described procedure for accurate image registration. Finally, we extend this approach through readily applicable options that integrate the calibration of the microscope system and provide validation strategies for image correction in order to create standardised, thorough, and reproducible approaches for multicolour STED image analysis.

Methods

Gold bead alignment samples

Stirring and heating to 50°C, 1.5 g polyvinyl alcohol (Mowiol 4–88, Sigma-Aldrich, Taufkirchen, Germany) was diluted in 10 mL distilled water. A colloid of gold nanoparticles of 80 nm diameter suspended in water (BBinternational, Cardiff, UK) was sonicated for 10 min. A volume of 10 μL of the gold colloid was diluted with 100 μL of the Mowiol 4–88 solution and 100 μL of the dispersion was pipetted onto a coverslip [22 × 22 mm²; thickness #1.5 (0.16–0.19 mm)]. The coverslip was spin-coated for 30 s at 4000 rpm, covered, and left to dry for 30 min. The coverslip was mounted onto a microscope slide with immersion oil appropriate for our imaging system (immersion oil type F, Leica Biosystems, Nussloch, Germany). The sample was left to dry for 5 min and then sealed with nail polish.

Multicolour bead samples

Fluorescent microspheres (TetraSpeck T7279, 0.1 μm diameter, Molecular Probes via Thermo Fisher, Dreieich, Germany) were prepared according to the supplier instructions. Briefly, the microsphere suspension was diluted 1:2 in distilled water resulting in a density of $\sim 9 \times 10^{10}$ particles mL^{-1} and 5 μL of this dilution were spread on a coverslip. After drying, the microsphere preparation was mounted on coverslides using an antifade reagent (ProLong Gold P36934, Molecular Probes via Thermo Fisher, Dreieich, Germany).

Immunofluorescence-labelling of cardiomyocytes

Murine ventricular myocytes were isolated as previously described (Wagner *et al.*, 2014). In short, mouse hearts were digested by collagenase type II (Worthington) via Langendorff perfusion. After ~7 min of digestion, the ventricles were carefully dissected followed by the addition of stopping buffer containing 10% bovine calf serum in order to arrest enzymatic digestion. Isolated ventricular myocytes were washed twice in stopping buffer before fixation and immunostaining.

For the preparation of dual-colour ryanodine receptor type 2 (RyR2) immunofluorescence stains, isolated ventricular myocytes were plated on laminin coated coverslips for 30 min and fixed with 4% PFA (10 min, RT) as previously described (Brandenburg *et al*, 2016). Primary antibodies were diluted 1:500 in blocking buffer containing 0.2% Triton X-100 and 10% bovine calf serum. For dual-colour staining of the identical RyR2 channel alpha-subunit, rabbit anti-RyR2 (HPA020028, Sigma-Aldrich, Taufkirchen, Germany) and mouse anti-RyR2 (clone C3-33, MA3-916, Thermo Fisher) were used. Cells were incubated overnight at 4°C with the primary antibody dilution, washed three times with blocking buffer and subsequently incubated with 1:1000 diluted secondary antibodies in blocking buffer (STAR635P goat anti-rabbit and STAR488 goat anti-mouse; Abberior GmbH, Goettingen, Germany). After three PBS washing steps, the samples were mounted on coverslides using an antifade reagent (ProLong Gold P36934, Molecular Probes).

Calculation of focal intensity distributions

Calculated focal intensity distributions are presented in Fig. S1 and referred to as 'calculated point spread functions (PSFs)'. An integral expression describing the focal intensity distribution of a high numerical aperture lens for arbitrary apodisations is given in (Keller *et al.*, 2007). Based on the vectorial diffraction theory, here it was used to describe the focal field distributions of each the excitation and STED depletion beams. The wavelengths were 594 nm for the excitation beam and 775 nm for the STED beam. Both incident beams were assumed to be circularly polarised. In addition, the STED beam featured a helical phase apodisation running from 0 to 2π (with the polarisation and helical phase apodisation having the same direction of rotation). The objective lens was aplanatic with a numerical aperture of 1.4 (oil). Lateral (X–Y) and axial (X–Z) sections of the focal intensity distribution were calculated numerically on a 1×1 μm² and a 1×2 μm² grid, respectively, with a pixel size of 10×10 nm² and displayed by a false colour map. The results were compared with images of 80 nm diameter gold beads scanned with the same STED microscope system at the corresponding wavelengths and phase apodisations.

STED microscope and image acquisition settings

All images were acquired using a commercially available multicolour STED microscope (Leica TCS SP8 STED 3X, Leica Microsystems GmbH, Wetzlar, Germany) equipped with a white light laser source operated in pulsed mode (78 MHz repetition rate) for fluorophore excitation and two STED lasers for fluorescence inhibition: one STED laser with a wavelength of 775 nm operated in pulsed mode with pulse trains synchronised to the white light laser pulses, and one continuous-wave STED laser with a wavelength of 592 nm. Excitation wavelengths between 470 and 670 nm were selected from the white light laser emission spectrum via an acousto-optical beam splitter (AOBS). All laser beams were focused in the cell sample with a wavelength corrected, 1.40 numerical aperture oil objective (HC PL APO 100×/1.40 OIL STED WHITE). The samples were scanned using the field-of-view beam scanner at uniform scanning rates and within specific scanning areas further specified below. Both the backscattered light and fluorescence from a given sample were detected by a photomultiplier tube (PMT) or the two built-in GaAsP hybrid detectors, respectively. The recorded fluorescence signal in the STED imaging mode was time-gated using the white light laser pulses as internal trigger signals.

The point spread functions (PSFs) were visualised by recording the backscattered light from 80 nm sized gold beads (see *Gold bead alignment samples* section) illuminated with two selectively picked wavelengths from the white light laser source (500 nm and 635 nm to represent the microscope's response function of the green and red colour channel, respectively) and the two STED lasers (592 and 775 nm). The built-in transmission photomultiplier tube (PMT) was used for detection. The reflected light was collected in the following detection windows: 490–510 nm for 500 nm excitation, 582–602 nm for 592 nm excitation, 625–645 nm for 635 nm excitation and 765–785 nm for 775 nm excitation. The PSF images with laser lines from the same colour channel were acquired simultaneously via line-sequential scanning. For lateral PSFs, a field of 1×1 μm² was scanned, and for axial PSFs, a field of 1×2 μm² was scanned. Each scan was performed at a scan rate of 600 lines per second and with the excitation and STED laser powers tuned to very low values using the microscope software (LAS AF), that is, <0.5% for the excitation laser wavelengths and <1% for the STED lasers, in general and to protect the microscope's detection units.

Two-colour fluorescence images of fluorescence-labelled murine cardiomyocytes (see *Immunofluorescence-labelling of cardiomyocytes* section) were acquired by sequential scans for each colour channel. These colour channels were defined as the 'green' colour channel (fluorescent dye: Abberior STAR488 with excitation at 500 nm and STED at 592 nm) and the 'red' colour channel (fluorescent dye: Abberior STAR635P with excitation at 635 nm and STED at 775 nm). For the red colour channel, a 'quasi-confocal' image of the green colour channel was recorded simultaneously by line-interleaved scanning. We define quasi-confocal by the signal of the green fluorophore being detected while the 775 nm STED laser is switched on. Fluorescence images were acquired at a scan rate of 600 lines per second, resulting in a pixel dwell time of 0.4 μs, and within a scan format of 1024×1024 px², and a pixel size of 22.73×22.73 nm². Fluorescence was detected with the microscope's hybrid detectors within detection windows of 515–560 nm and 650–700 nm for the green and the red colour channel, respectively. The fluorescence images were obtained with 16-fold line averaging but no frame accumulation. For the STED images of the green colour channel,

fluorescence time-gating was set to 1.5–6.0 ns; for the red colour channel, fluorescence time-gating was set to 0.5–6.0 ns.

Moreover, the multicolour fluorescent TetraSpeck bead samples (see *Multicolour bead samples* section) were imaged using the exact same settings as described for dual-colour STED imaging of immunofluorescence labelled isolated cardiomyocytes (see previous paragraph in *STED microscope and image acquisition settings* section).

Image processing for registration

All image processing steps were conducted using custom-written scripts and mathematical functions using MATLAB (The MathWorks, Inc., Natick, MA, USA). All functions used for the image processing were implemented in the MATLAB software (version R2010b or higher). The MATLAB script, further specified in *Image registration protocol, step-by-step* section, features the calculation of the pairwise cross-correlation between the calibration sample images and/or actual sample images. The relative two-dimensional offset vector between images is determined by maximisation of the respective cross-correlation via variation on a grid in the Fourier space. In relation to its reference image, the image is thereby circularly shifted by the calculated offset vector. Finally, the corrected images for each colour channel are similarly cropped along the borders in order to be directly overlaid and used for further quantitative image analysis. The image processing scripts described here are available for download (Supplemental File SF1).

Validation of image registration

To quantify the corrective effect of the image registration protocol, the spatial overlap between colour channels of the two-colour cardiomyocyte calibration sample (see the sample preparation protocol described above, *Immunofluorescence-labelling of cardiomyocytes*) was assessed. To this end, the colour channel signal intensity distributions in the *X*- and *Y*-direction were extracted from STED image overlays of (1) the unprocessed image data, (2) the linearly aligned image data and (3) the registered image data, respectively by adding up the individual colour channel's pixel intensities along the *X*- and *Y*-direction of a rectangular region encompassing a single protein signal structure. Thirty such regions per overlay image were analysed, thereby evaluating the same regions in each the original, linearly aligned, or registered image data, originally obtained from individual cardiomyocyte calibration samples. The signal intensity distributions were fit with a Gaussian peak function using MATLAB and the distance between the Gaussian peaks was determined, yielding the colour channel offset in the *X*-direction (in case of the pixel intensity add-up in the *Y*-direction) and the colour channel offset in the *Y*-direction (in case of the pixel intensity add-up in the *X*-direction). The distances between colour channel signal peaks were determined as the mean ± standard deviation of the norm of the vector comprising the colour channel offset in the *X*- and *Y*-direction of a specific signal peak. For the determination of the distances between colour channels, further signal peaks from four additional cells in the cardiomyocyte calibration sample (each 30 peaks per cell) were analysed. The distances were denoted as (1) d_{raw} for the unprocessed image data, (2) d_{lin} for the linearly aligned image data and (3) d_{reg} for the registered image data. The obtained individual values for the *X*- and *Y*-coordinates of d_{raw}, d_{lin} and d_{reg} were plotted in two-dimensional scatter plots. Statistical significance of the difference between d_{lin} and d_{reg} was assessed using the two-sided Mann–Whitney–Wilcoxon *U* test that is integrated in MATLAB via the function 'ranksum'. The data sample size for each d_{lin} and d_{reg} amounted to 150 signal peaks from 5 different cardiomyocytes (i.e. 30 extracted signal peaks per cell). Statistical testing yielded a p value of $3.7\times e^{-11}$ and was denoted as (***) – highly significant ($p < 0.001$) in Figure 4.

Results

Performance and documentation of the STED microscope system

To obtain the highest level of resolution possible through sub-diffraction STED imaging, it is necessary to align and calibrate the microscope, ideally upfront. Consequently, because STED is a targeted superresolution method leading to direct image generation without any secondary image reconstruction steps, it is particularly important that all excitation and STED laser beams are optimally aligned.

For this, commercial STED microscope systems provide a user-friendly auto-alignment option through their proprietary software. In addition, the incident microscope status can be documented independently by users. This status documentation includes the spatial alignment of the laser beams as well as the individual beam profiles. Specifically, the intensity distributions of the laser beams in the focal plane of the objective can be documented. To record the point spread function (PSF) for each illuminating laser beam of a given STED system, a standardised alignment sample is needed. Here, we use an alignment sample of nanosized gold beads prepared as described in *Gold bead alignment samples* section. The backscattered light from the individual gold beads is detected in the reflection pathway of the microscope, for example using a photomultiplier tube (PMT). It is important to note that any backscattered signal originating from the gold beads will be very bright, so in order to protect the PMTs and the sample, generally a low illumination power in the range of a few μW is used (measured in the back focal plane of the objective). Using an alignment sample of nanosized gold beads has the following advantages:

(1) Gold beads do not bleach during laser illumination and are thus ideally suited for multiple sequential scanning procedures.
(2) Gold beads reflect the incident light of a broad range of wavelengths and can hence be used to monitor the PSFs of all laser lines used in a given optical setup.
(3) Gold bead samples can be stored over extended periods (>1 year) without a loss of quality.

Principally, alternative approaches to prepare samples for spatial laser beam alignment exist as follows and can be considered. First, multicoloured fluorescent beads (see *Multicolour bead samples* section) can be recorded in the actual fluorescence pathway of the microscope. Second, fluorescent semiconductor nanocrystals (quantum dots; Reed *et al.*, 1988); and third, labelled proteins (e.g. cytoskeletal proteins such as actin) can be used as fluorescent alignment samples. The expected benefit of performing the laser beam alignment with exogenous samples recorded in the microscope's fluorescence pathway comprise their fluorescence detection analogous to the actual experimental sample. This is because the PSFs of fluorescent alignment samples can be recorded with overall similar illumination and detection parameters. Also, fluorescent polystyrene beads can be doped with up to four different dyes. However, these beads are photobleached during each sequential scan, which can significantly compromise the alignment procedure. In addition, the spectral properties of the dyes decorating the beads will not necessarily match the given microscope configuration, that is, the available laser beam wavelengths and/or detection windows.

Further considering advantageous Qdot properties, these are very small, photostable and feature a broad excitation spectrum and narrow emission bands (Walling *et al.*, 2009; Wegner & Hildebrandt, 2015). Yet, quantum dots show intermittent fluorescence ('blinking'), which makes them less suitable for the beam alignment procedures. In particular, for STED application, while blinking can be suppressed by simultaneously illuminating quantum dots with the excitation and the STED laser (Hanne *et al.*, 2015), random blinking prevails during scanning with a single laser line.

In general, for alignment samples labelled with different fluorophores it is possible to choose the same fluorophores that are also used for the actual experimental sample. For example, fluorescence labelling of actin via the cytoskeletal toxin phalloidin yields multicolour structures with only very small fluorescence tags. Nevertheless, fluorescence labelled proteins are prone to photobleaching and to photodamage caused by the thermal load conveyed by the illuminating laser beams.

In summary, for laser beam alignment gold bead samples offer clear advantages, generally preferable to fluorescent samples. Consequently, we used gold bead samples for calibration of our STED microscope system and as the basis to standardise the daily characterisation of the microscope status as described below.

Figures 1(A) and (B) show the PSFs of the laser beams that we acquired with a commercially available microscope system (see *STED microscope and image acquisition settings* section) for a typical two-colour imaging scheme, that is, using two excitation laser lines and two different STED beams. For the measured gold bead PSFs, we chose the same excitation and STED wavelengths that we also use to image the actual two-colour samples. Specifically, for the 'green' colour channel, the wavelengths are 500 nm for excitation and 592 nm for STED – that is, the typical illumination parameters for the dye Abberior STAR488. For the 'red' colour channel these wavelengths are 635 nm for excitation and 775 nm for STED – that is, the typical illumination parameters for the dye Abberior STAR635P.

Regarding the laser beam PSFs, the following criteria are generally considered for optimal STED performance: (1) the laser beam shape, (2) the quality of the central minimum of the STED beam, (3) the polarisation of the STED beam and (4) the laser beam alignment (overlay). Criteria (1)–(3) are further elaborated for optimisation in custom-built and particularly open STED microscopy systems in the Supplementary Information (Supplement 1). Here, we describe and characterise the laser beam alignment (criterion 4).

For multicolour STED imaging with two or more STED 'doughnuts' sufficient spatial alignment of all excitation PSFs can be assumed if state-of-the-art high-end objective lenses are used. In addition, the precise alignment of two or more applied STED 'doughnuts' is of critical importance for image resolution. Because the minimum intensity regions of the STED beams define the central position of the detectable fluorescence signal, any displacement will necessarily cause an inadvertent shift between the different colour channels. Ideally, in the lateral imaging plane, the intensity maximum of the excitation laser PSF aligns perfectly with the intensity minimum of the STED laser PSF, resembling the overlay of the numerically calculated PSFs shown in Figure S1(A). Along the axial planes (both *X*–*Z* and *Y*–*Z* plane) the intensity maximum of the excitation laser PSF is centred between, parallel to, and at the same axial position as the two STED PSF maxima. This ideal axial alignment is exemplified by the overlay of the numerically calculated axial PSFs as shown in Figure S1(B).

Figures 1(A) and (B) display experimentally obtained PSFs from gold beads using either the green or red colour channel as described above and in the corresponding *STED microscope and image acquisition settings* section (for clarity, we show only the lateral PSFs). Corresponding axial PSFs can be found in Figures S2(A) and (B), respectively. The expected alignment of the excitation and STED beams is shown for each colour channel in Figures 1(A) and (B), respectively. The graphs in Figures 1(A) and (B) show the normalised intensity profile measured along the double-arrow line indicated in the single beam PSF images. For the green channel, the intensity

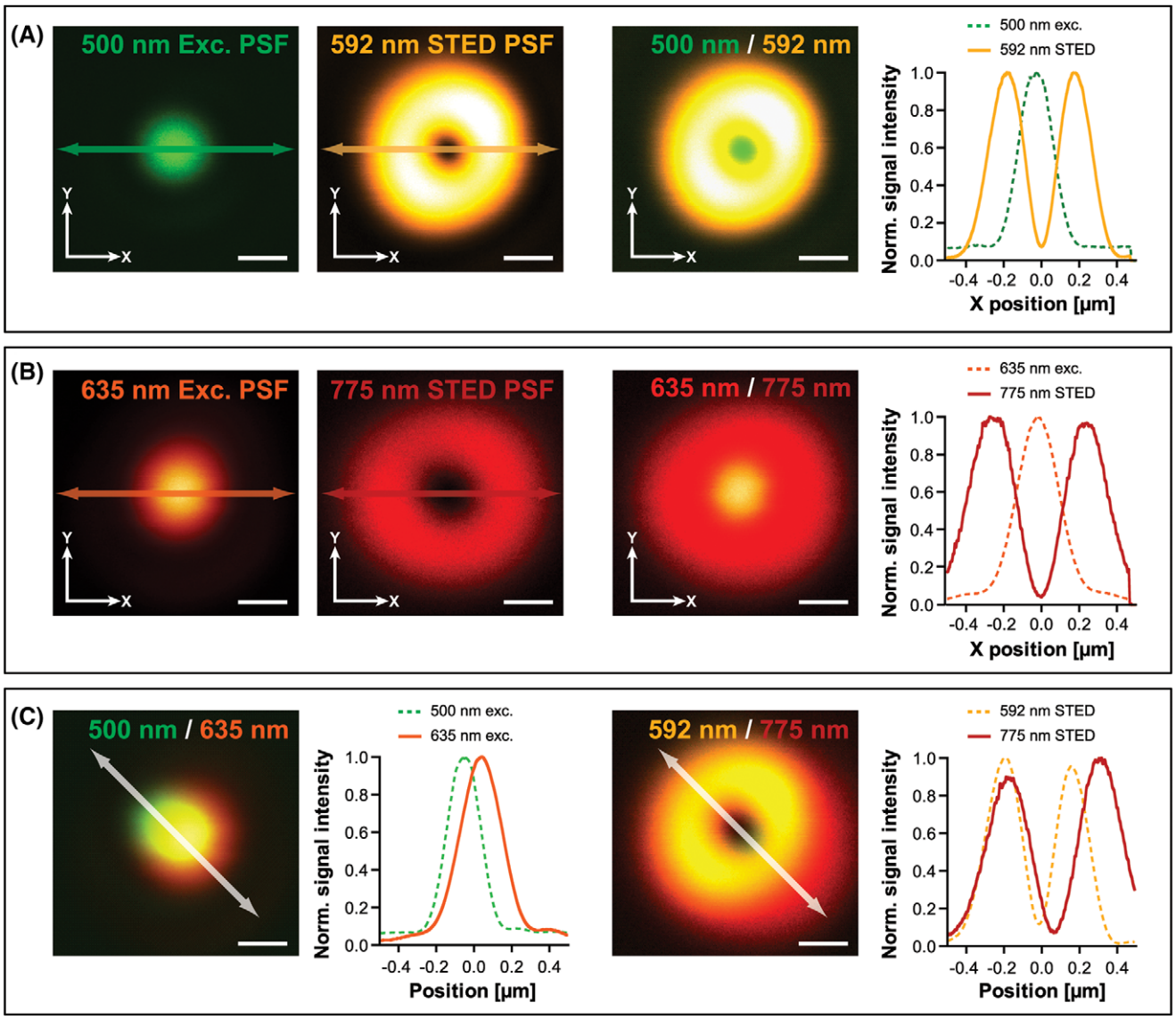

Fig. 1. Measured point spread functions (PSFs) from scanned gold beads. Shown are the PSFs of the excitation and STED laser beams at different wavelengths. Both the excitation and STED beams are circularly polarised and use an Airy disk amplitude profile; the STED beam is additionally modulated by a helical phase from 0 to 2π. For select PSFs, the normalised signal intensity distribution was obtained from individual line profiles indicated by double arrows in each image. All scale bars: 200 nm. (A) Measured lateral PSFs from scans of 80 nm gold beads illuminated with the excitation and STED laser of the green colour channel. From left to right: PSF of the 500 nm excitation laser (in green, dashed line); PSF of the 592 nm STED laser (in yellow, solid line); overlay of excitation and STED laser PSFs; normalised signal intensity distribution obtained from line profiles along the double arrows depicted in the single beam PSFs. (B) Measured lateral PSFs from scans of 80 nm gold beads illuminated with the excitation and STED laser of the red colour channel. From left to right: PSF of the 635 nm excitation laser (in orange, dashed line); PSF of the 775 nm STED laser (in red, solid line); overlay of excitation and STED laser PSFs; normalised signal intensity distribution obtained from line profiles along the double arrows depicted in the single beam PSFs. (C) Pairwise PSF overlays of the corresponding excitation beam PSFs and STED beam PSFs shown in (A) and (B) and the normalised intensity distributions obtained by line profiles along the double arrows depicted by the indicated PSF overlays.

maximum of the excitation laser PSF and the intensity minimum of the STED laser PSF show an average displacement of 33.1 nm (Fig. 1A); for the red channel, the average displacement amounts to 23.7 nm (Fig. 1B). Note, although this displacement may cause a slight decrease in signal brightness, it will not critically affect the image offset between the green and the red channel. This is because the pairwise displacement between the excitation beam and its corresponding STED beam is of the same order as the pixel size typically chosen to fulfill the Nyquist criterion for a

microscope setup with an average image resolution of 40–50 nm.

Even more important for multicolour STED imaging is the lateral overlay between the two STED laser beam PSFs, which we assess in Figure 1(C). For quantification of the displacement between the PSFs, Figure 1(C) displays the signal intensity distributions obtained from line profiles drawn along the direction of the apparent maximal offset between PSFs as indicated by the tilted double arrows in the depicted PSF images. Both offsets are significant: the maximum offset between the intensity maxima of the excitation beam PSFs amounts to approximately 85 nm; for the two STED beams, the offset between the central intensity minima amounts to approximately 76 nm. This corresponds to an offset of about four times the typical pixel size, which is highly undesirable because it causes a sizable mismatch between the colour channels and calls for immediate correction, that is, through additional image processing.

Hence, to approach a general strategy for corrective image processing, a one-dimensional approach to determine image offset, for example between two STED beam PSFs will not provide sufficient data for reliable image registration. In other words, simply translating the PSF offset from the gold bead measurements into a spatial constant to correct for the image shift between the two-colour channel measurements will not adequately account for more complex causes of image mismatch. Additional factors including the inherent sample and dye properties, the specific detector pathway, dynamic effects from bleaching, random drift of components in the optical light path, and relative sample drift may occur. This implies that accurate image registration will depend significantly on reliable input parameters, which can be applied for each individual image or each coherent study group of images as appropriate.

Sample drift, in particular, can be a temporally and spatially highly variable cause of image mismatch. However, sample drift can be difficult to quantify, particularly throughout all images within or between different study groups. Notably, information about the specific sample drift that occurs during each individual scan of a given sample is contained in the set of the acquired images. This is why an image registration procedure performed separately for each set of two-colour images contains potentially advantageous information, which can be readily used as input calibration data and from each unprocessed image of the actual experimental sample.

In summary, for reliable and reproducible multichannel imaging with several STED beams, and to keep track of the actual microscope performance, monitoring and recording the displacement between the applied STED doughnuts is important. A microscope alignment check-up performed prior to the actual image acquisition on the day of the experiment will provide direct feedback about the technical performance quality of the microscope and, on a long-term basis, assist problem solving in case of questionable or deteriorating image data. In addition, it will significantly increase image reproducibility and the confidence in any subsequent image analysis.

Because of potentially challenging (described above) and inherent factors that are difficult to control – such as lens imperfections, ambient air flow, and heat transfer to the objective during sample illumination – displacement between two or more colour channels can never be fully eliminated. Even if small by standard convention, at the nanometric scale of a given STED microscope this can lead to a significant colour channel offset, which compromises any subsequent correlative STED image analysis. On the other hand, disadvantageous offset between different colour channels can be corrected by proper image registration following image acquisition, which can be a key strategic element to reproduce multichannel images based on several STED beams. Consequently, we developed a corrective strategy for image registration that relies on an explicitly described image acquisition mode and systematically matches different colour channels for experimentally obtained images.

Mode of STED image acquisition for correction

For image registration, two imaging steps are required. The first step comprises a simultaneous scan of the red STED channel and the green quasi-confocal channel of a *calibration sample*; 'quasi-confocal' describes the acquisition of fluorescence emitted by the green dye, which was excited and detected with the appropriate wavelengths but with the 775 nm STED laser switched on. Here, an abundant biological calibration sample was used. The ryanodine receptor type 2 (RyR2), which functions as an intracellular calcium release channel, was labelled with both a red and a green fluorescent dye in the same sample (Fig. 2A). The second step comprises a simultaneous scan of the experimental biological sample in the red STED channel and the green quasi-confocal channel. Next, this simultaneous scan is followed by a sequential scan in the green STED channel of the *actual* sample (Fig. 2C). Of note, during the calibration and experimental imaging steps each the respective *calibration* sample or the *actual* sample (the bona fide experimental sample) are described.

The first imaging step (the simultaneous scan of the calibration sample; see Fig. 2A) yields a red STED image and a green quasi-confocal image of the same protein structures, the cardiac RyR2 channel protein, which is typically arranged in a pattern of transversal striations as shown. These two images are used to estimate the assumed constant channel offset vector. This vector will describe the offset between the centre of the green excitation and the red STED PSF if there is no STED effect of this laser on the green fluorophore. In principle, this offset is due to chromatic aberrations and suboptimal system alignment. The protocol determines the offset vector by aligning the red STED image with the green quasi-confocal image via maximisation of the cross-correlation between the two images (Fig. 2B). As important prerequisite, it is

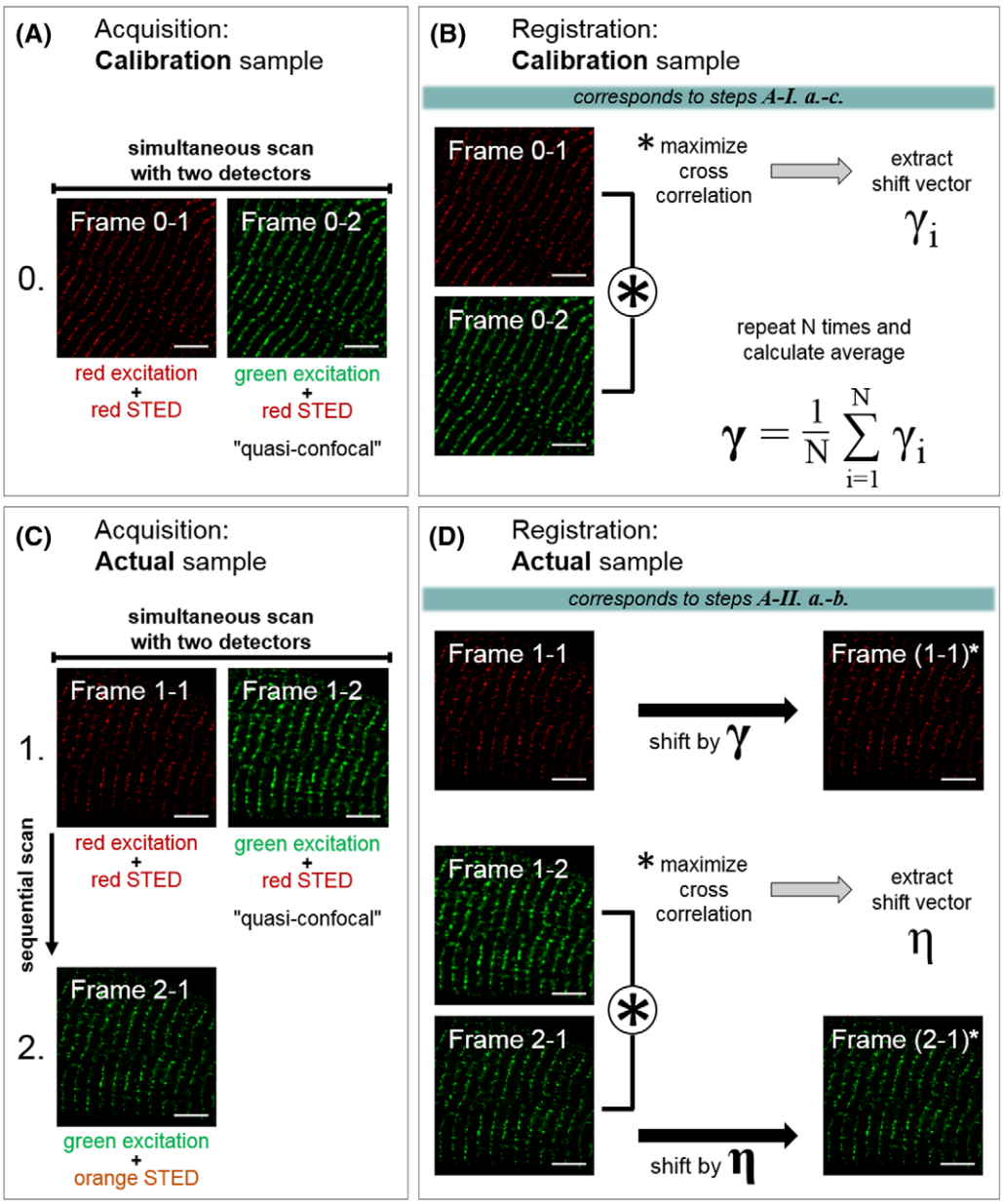

Fig. 2. Schematic of the image acquisition procedure used for corrective image processing. (A) Image acquisition scheme for the two-colour calibration sample. Frame 0–1 and frame 0–2 are recorded simultaneously; the red and green excitation laser, as well as the red STED laser are switched on throughout the entire scan. Frame 0–1 is the image detected in the red colour channel; frame 0–2 is the image detected in the green colour channel. (B) Image registration scheme for the two-colour calibration sample images acquired as described in (A). Figure 2 (B) corresponds to steps A-Ia–c (refer to *Image registration protocol, step-by-step* section): Frames 0–1 and 0–2 are registered using an algorithm that maximises the cross correlation of the two images. The image registration of the two colour channels of the calibration sample yields the shift vector γ_i for each acquired set i of calibration sample images. The registration procedure is repeated N times and the average shift vector γ is calculated as the arithmetic mean of the N obtained γ_i. (C) Experimental image acquisition scheme for the actual two-colour sample. Frame 1–1 and frame 1–2 are simultaneously obtained in the same manner as frame 0–1 and frame 0–2 described for (A). In addition, frame 2–1 is obtained by a subsequent scan. For this, the green excitation laser and the red STED laser are switched on and the emitted fluorescence signal is collected in the green colour channel. (D) Image registration scheme for the actual two-colour sample images acquired as described in (C). Note: Figure 2(D) corresponds to steps A-IIa and b (refer to *Image registration protocol, step-by-step*): Frame 1–1 is shifted by the mean shift vector γ that was obtained as described in (B), yielding the shifted frame 1–1*. Frames 1–2 and 2–1 are registered by maximisation of the cross correlation, yielding the shift vector η. Finally, frame 2–1 is shifted by η, resulting in the shifted frame 2–1*. Frames 1–1* and 2–1* are used for further image analysis.

necessary that the calibration sample displays bright and distinct signals of the same structure in both the red and the green channels.

In general, there are two categories of samples that are suitable as calibration samples. The first category comprises biological calibration samples, for example, cardiomyocytes in which RyR2 subunit proteins are decorated with two fluorescent dyes as mentioned in the last paragraph and described in the *Methods* section, titled 'Immunofluorescence-labelling of cardiomyocytes'. Additionally, protein A or protein G conjugated beads can be used if the same secondary antibodies and fluorescent dyes as in the actual sample are coupled. The resulting multicolour spheres will contain approximately the same fluorescence marker configuration as that of the actual sample. Compared to the calibration sample featuring the multilabelled protein of interest, the protein A/G conjugated beads are less expensive and can generally be used with different dye combinations. Yet, conjugated beads will not provide the same spatial detail as a multicolour labelled biological protein structure in the actual sample. This can be a major disadvantage if the colour channel offset is not isotropic across the region of interest used for image acquisition. In addition, samples of protein conjugated beads are typically thin (<1 μm) and may not reproduce the original optical aberration that arises micrometres deep inside a complex biological sample. In particular, for STED microscopy, aberrations due to thicker samples need to be carefully considered.

The second category of potential calibration samples comprises exogenous multicolour fluorescent beads, fluorescence labelled actin filaments, or quantum dots (see *Performance check and documentation of the microscope system* section). In general, exogenous calibration samples are advantageous because they don't require different antibodies for multicolour labelling. The calibration sample may basically use any structure decorated with dyes that exhibit similar absorption and emission spectra as those used for the actual sample.

However, a biological calibration sample that uses exactly the same dyes as the actual sample and in which an epitope of the same target protein as in the actual sample is decorated, is preferable to directly detect a displacement between the image scans described above (see Fig. 2). Ultimately, the biological calibration sample closely resembles the actual sample including its spectral properties, the characteristics of the fluorescently labelled structure and the sample thickness.

Hence, as calibration sample we used fixed isolated cardiomyocytes, where the RyR2 channel was labelled with two different primary antibodies, one produced in mouse and one in rabbit. RyR2 signals were detected by distinct anti-mouse and anti-rabbit secondary antibodies each conjugated to a fluorescent dye, STAR488 and STAR635P, respectively. Thus, the calibration sample used here represents a truly biological, nontrivial sample, because the RyR2 signal spots show highly variable dimensions and overall complex spatial patterns. Here, we used a 'classical' sandwich approach using primary and secondary antibodies, because this represents the most widely used labelling technique. However, if applicable, primary labelling of the protein of interest, for example by directly labelled primary antibodies or nanobodies, can be advantageous.

The second imaging step, comprising both a simultaneous and a sequential scan of the actual sample shown in Figure 2(C), will yield three distinct images: a red STED image of protein epitope 1, a green quasi-confocal image of protein epitope 2 and a green STED image of protein epitope 2. Here, the red and the green STED images are essential for co-localisation studies. The additional quasi-confocal green image of protein epitope 2 will be used to align the images as described in detail below.

For general protocol purposes, we define the following imaging steps and corresponding acquisition settings outlined in Figure 2 as standard:

- Frame 0–1: the red STED channel of the calibration sample, that is, the red excitation and red STED laser are switched on, with fluorescence detected in the red detection window.
- Frame 0–2: the green channel of the calibration sample simultaneously recorded with Frame 0–1, that is, the green excitation and red STED lasers are switched on, with fluorescence being detected in the green detection window.
- Frame 1–1: the red STED channel of the actual sample, that is, the red excitation and red STED lasers are switched on, with fluorescence detected in the red detection window.
- Frame 1–2: the green channel of the actual sample is simultaneously recorded through Frame 1–1, that is, both the green excitation and red STED lasers are switched on, with fluorescence detected in the green detection window.
- Frame 2–1: the green STED channel of the actual sample consecutively recorded after frames 1–1 and 1–2, that is, the green excitation and orange STED lasers are switched on, with fluorescence detected in the green detection window

Taken together, five individual images are recorded, which is sufficient to represent the entire data set necessary for two-colour STED image registration. To allow for quantitative comparison, all images are recorded with the same acquisition parameters and using the same field of view of the total available scan field (note: chromatic aberrations in distinct regions of the scan field can differ and hence panning is generally not recommended). As outlined above, the calibration sample images are acquired prior to imaging of the actual sample to capture potential changes due to sample drift as well as chromatic aberrations of the microscope system. Although a singular calibration measurement per day may be sufficient, extended high-volume imaging sessions may require additional measurements for accurate image quantification.

Image registration protocol, step-by-step

Prior to image registration, the following points need to be generally confirmed: does the red STED laser exert any photoswitching effect on the green fluorescent dye? For protocol purposes, we foresee two classes of outcome procedures referred here as case A versus B. Case A applies if the red STED laser does not affect the green fluorescent dye. In contrast, case B applies if the red STED laser does affect, that is, de-excites, the green fluorescent dye. Depending on the two different cases, the registration procedure needs to be further adjusted as specified below (*Case A* and *Case B*, respectively). To evaluate the effect of the red STED laser on the green dye, two images of the green fluorescent dye in the actual sample are recorded – ideally simultaneously, via line-sequential scanning, to rule out artefacts from drift and bleaching. In the first image, only the green excitation laser is switched on. In the second image, both the green excitation laser and the red STED laser are switched on. If the signal intensity in the second image decreases significantly, that is, >10–20% of the confocal signal, a STED effect is present. Although a decrease in signal intensity is sufficient as a criterion to verify the STED effect, a significant improvement in image resolution is the most direct way, but may be masked, for example by the inherent size of the underlying structure.

Case A: the 'red' STED laser does not affect the 'green' fluorescent dye

In this case frames 0–2 and 1–2 display confocal images, which are used as reference frames to align frames 1–1 and 2–1, respectively. The image registration procedure is executed according to the following scheme:

A-I. Use the images of the calibration sample:

(a) Shift frame 0–1 onto frame 0–2 by maximising their cross-correlation; document the optimal shift vector, that is, γ_i for reference.
(b) Repeat step A-I.a for different spots I using the same calibration sample.
(c) Calculate the arithmetic mean from all obtained vectors γ_i and denote as γ.

A-II. Use the images of the actual sample:

(a) Shift frame 1–1 by the mean vector γ to yield the shifted frame 1–1*.
(b) Shift frame 2–1 onto frame 1–2 by maximising their cross-correlation to yield the new shifted frame 2–1*; document the actual shift vector η.
(c) Cut frames 1–1* and 2–1* along the border by the maximal absolute value of γ and η to avoid peripheral shifting artefacts.
(d) After cutting, the shifted frames 1–1* and 2–1* will be used for further analysis.

Note: Step A-I is illustrated in Figure 2(B) and A-II is illustrated in Figure 2(D).

In 'open' customised microscope systems, it is advisable to image the calibration sample repeatedly during the image acquisition session of the actual sample if imaging sessions are relatively long. Thereby, possible temporal variations in the displacement between the red STED and the green excitation beam can be recorded and corrected for. Here, commercial systems usually offer a beam alignment procedure through proprietary software. If auto-alignment is an option, the calibration sample can be imaged right after the auto-alignment was executed. Assuming a reliable auto-alignment procedure, imaging the actual sample will capture the beam alignment status once or after each auto-alignment, which can be recorded through the obtained image data of the calibration sample.

An alternative strategy for image registration described as case A might be additional embedding of fluorescent beads in the actual biological sample (as described in Donnert *et al.*, 2007; Preibisch *et al.*, 2010). This strategy, however, has important caveats. First, the preparation of a fluorescent bead sample might be incompatible with the requirements for the preparation of the actual biological sample given by the embedding medium and the staining procedure. Second, for sample imaging deeper inside the biological specimen, fluorescent beads need to be incorporated within the volume of the specimen, an invasive approach, which might be undesirable. Third, the density distribution of the fluorescent beads in all three dimensions of the sample is difficult to control and could, for example, be either too sparse for image registration or too dense and thus interfering with the actual sample's signal structure of interest. Finally, some effort is necessary to embed the fluorescent beads in every sample throughout the study in a reproducible way.

In summary, the image registration protocol circumvents the laborious and perhaps not practicable preparation of biological samples with embedded fluorescent beads as reference for registration. Because the image registration protocol is based exclusively on the obtained image data, it generally avoids gross manipulation of the biological sample and related sources of artefact entirely.

Case B: the 'red' STED laser affects the 'green' fluorescent dye

This case is displayed in frame 1–2 by the fluorescence signal of the green fluorophore, which is partially depleted by the red STED laser. As a result, imaging of the calibration sample is not necessary and only the images from the actual sample are needed for image registration, because both the red fluorescence signal in frame 1–1 as well as the green fluorescence signal in frame 1–2 are localised to the same intensity minimum

of the red STED laser. This means that frames 1–1 and 1–2 are intrinsically aligned. Thus, if case B applies, the image registration procedure can be simplified as described by the following scheme:

B-I. Use the images of the actual sample:

(a) Shift frame 2–1 onto frame 1–2 by maximising their cross-correlation to yield the shifted frame 2–1*; document the respective shift vector η.
(b) Cut frames 1–1 and 2–1* along each border by the maximal absolute value of η to avoid peripheral shifting artefacts.
(c) After cutting, for further analysis, the unshifted frame 1–1 and the shifted frame 2–1* will be used.

For procedural clarity, Figure 3 summarises the main steps of the image registration protocol described in this section in the form of a decision tree for cases A and B.

Validation of the registration protocol

Following image registration, we validated the protocol by estimating the error and hence the limit of any subsequent quantification and interpretation of the experimental data. To this end, we propose a set of descriptive parameters that can be extracted from the data in order to characterise and validate the goodness and aptness of the image registration. Ideally, these parameters are provided with the corrected image data, that is, for a research manuscript. Here, exemplary parameters from the above described image data are presented to compare the precision of the image registration against other common procedures.

To extract the descriptive parameters, it is important to generate each the image for the calibration and actual sample in the same fashion as described above. Accordingly, the same nomenclature introduced in *Mode of STED image acquisition for correction* section applies; that is, for the calibration sample, we use frames 1–1, 1–2 and 2–1 as shown in Figure 2(B). Hence, the image registration procedure per se is the same as described in *Image registration protocol, step-by-step* section. For the calibration sample, this yields each a set of unprocessed and registered images, which are overlaid and further analysed as described next. Moreover, to estimate the registration procedure quality, we use the two-colour calibration sample described above: fixed murine cardiomyocytes stained for RyR2 and imaged via indirect immunofluorescence using the fluorescent dyes STAR488 and STAR635P for the green and red colour channel, respectively (for details of the sample preparation, see *Immunofluorescence-labelling of cardiomyocytes* section).

Notably, in cardiomyocyte samples, we did not observe any photoswitching effect by the 775 nm STED laser based on the dye STAR488 in the green channel. Thus, for the actual sample stained with two different fluorophores, case A (see *Image registration protocol, step-by-step* section) applies and the corresponding image registration protocol was performed. To validate the precision of the image registration procedure, we used the cardiomyocyte sample with the same protein structure decorated with two different fluorophores. Accordingly, step I of the registration procedure (case A) is analogous to step II and is not required for this specific case. Consequently, the red channel image is not shifted by any vector. Accordingly, in Figure 4, we refer to the 'registered and corrected red image' (frame 1–1*) and 'registered and corrected green image' (frame 2–1*) as compared to the 'original red image' (frame 1–1) and 'original green image' (frame 2–1). Using this set of images, as described above, next the registration aptness can be validated through three distinct protocols described next.

First, a uniform image offset across the whole field of view is verified through one single scan. For this, the original image frame obtained from the calibration sample can be divided into smaller subimages, which are processed separately according to the image registration protocol. This procedure is repeated throughout different regions of interest in the calibration sample. Individually obtained shift vectors η_i are documented and compared between the main images and the subimages. For quantification, the standard deviation of each component and for all obtained shift vectors is calculated and concatenated as vector $\delta\eta_1$. For a uniform image offset across the whole field of view, $\delta\eta_1$ has to be below the size of 1 pixel in each dimension. For example, for a given cardiomyocyte sample, we divided the calibration sample images into four quadrants of equal size and compared the shift vectors between ten different cardiomyocytes. Here, the discrepancy between the shift in the quadrants and the total image was $\delta\eta_1 = 0.29, 0.0$ px, corresponding to 6.6 and 0.0 nm, in the *X*- and *Y*-direction, respectively, thus confirming a uniform image offset.

Second, we verified that the image offset is uniform for different regions of interest within the same sample. To this end, the shift vectors η from different regions of interest were compared by component-wise calculation of their mean (concatenated in the vector η_2) and standard deviation (concatenated in the vector $\delta\eta_2$). Again, a uniform image offset can be assumed if this standard deviation $\delta\eta_2$ is below the size of 1 px in each dimension. We performed this analysis for ten different regions of interest, each representing one cardiomyocyte in our calibration sample and found the mean shift vector $\eta_2 \pm \delta\eta_2$ to be -4.33 ± 0.47 and -2.00 ± 0.82 px, corresponding to -98.3 ± 10.7 and -45.4 ± 18.6 nm in the X- and Y-direction, respectively, which indicates uniform image offset.

Third, to confirm registration accuracy the original images of the calibration sample are compared with the registered images. To this end, the red and green image channels of both the unprocessed as well as the registered images are overlaid. This results in two image overlays from which corresponding discrete signal spots are extracted and their signal intensity distributions are determined. This can be done by either

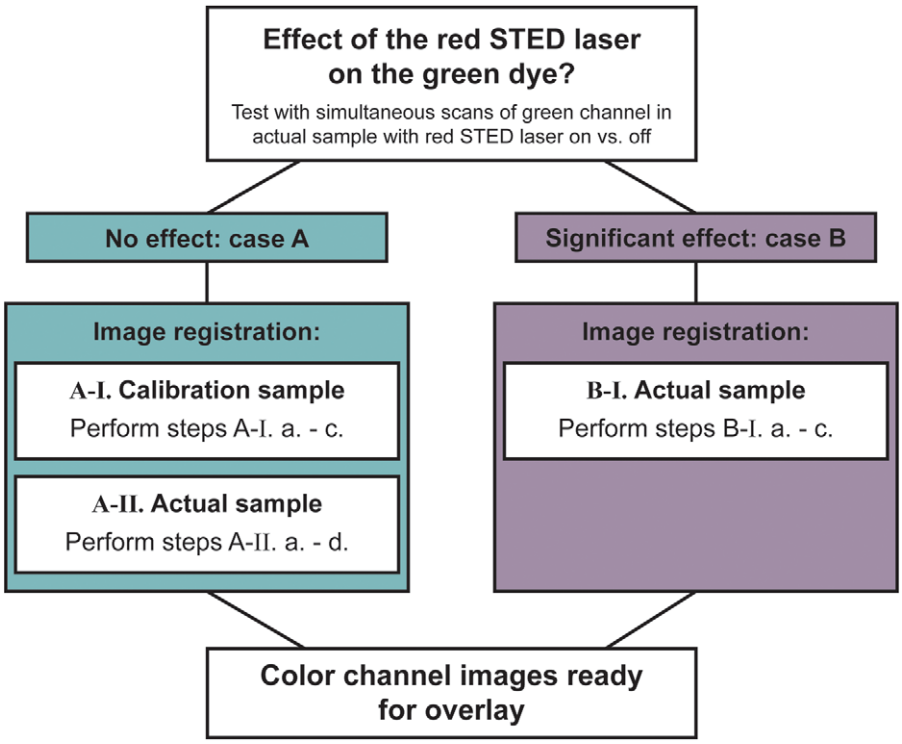

Fig. 3. Decision tree visualising the proposed image registration protocol and summarising the two different cases A versus B and the corresponding image processing steps.

averaging the signal along one dimension within a boxed region around the signal spot or by a line profile through the signal spot. For the latter method, the signal intensity is averaged along a line profile of about 10 pixels in width or large enough to avoid artefacts due to signal noise. The distance between the average peak intensity of the red and the green signal spot is denoted for the original data and the processed data, respectively. This procedure is then repeated for several similar signal spots in the recorded field of view and also for different regions of interest in the calibration sample. From the obtained set of peak distances, the mean distance and the standard deviation are calculated in both dimensions and for both scenarios: the mean peak distance d_{raw} for the original images versus the mean peak distance d_{reg} for the registered images. From this, the mean improvement of signal overlap can be derived as the difference between the peak distances before and after image processing.

To compare the quality of the proposed image registration protocol, we evaluated the degree of colour channel overlap based on linear colour channel alignment. Image registration based on this 'linear alignment' was performed by assessing the mean displacement vector ξ between the red STED (i.e. frame 1–1) and the green STED image (i.e. frame 2–1) from different spots in the cardiomyocyte calibration sample. Accordingly, shifting the green STED image by ξ was used for correction (resulting in the corrected frame 2–1**), and using frame 1–1 and frame 2–1** for image overlays and extraction of the signal peak distances d_{lin}. In short, ξ was determined from the five two-colour image scans of the cardiomyocyte calibration sample and calculated as $\xi = 8 \pm 14, 2 \pm 6$ px, which indicated considerable variance and a relatively large colour channel offset between the red and the green STED image. For comparison, the shift vector γ between the red STED image and the green quasi-confocal image determined from sequentially scanned images as described in *Image registration protocol, step-by-step* section amounts to $\gamma = 0 \pm 1, -4 \pm 1$ px. Taken together, comparison with the linear alignment demonstrates a profound effect of the displacement between the doughnut-shaped STED laser beams and confirms that the simpler linear alignment procedure for image registration will not sufficiently correct for this displacement.

As example, we compared the colour channel overlay images of the two-colour cardiomyocyte calibration sample for the following three cases: (1) the original, unprocessed image data (displayed in Fig. 4A), (2) the linearly aligned data (displayed in Fig. 4B) and (3) the registered and corrected data according to the proposed registration protocol (displayed in Fig. 4C). Figures 4(A)–(C) each display an overview image of an individual dual-labelled cell from the cardiomyocyte calibration sample and two image magnifications corresponding to the marked regions in the overview images, namely: an organotypic sequence of signal spots along a cardiomyocyte

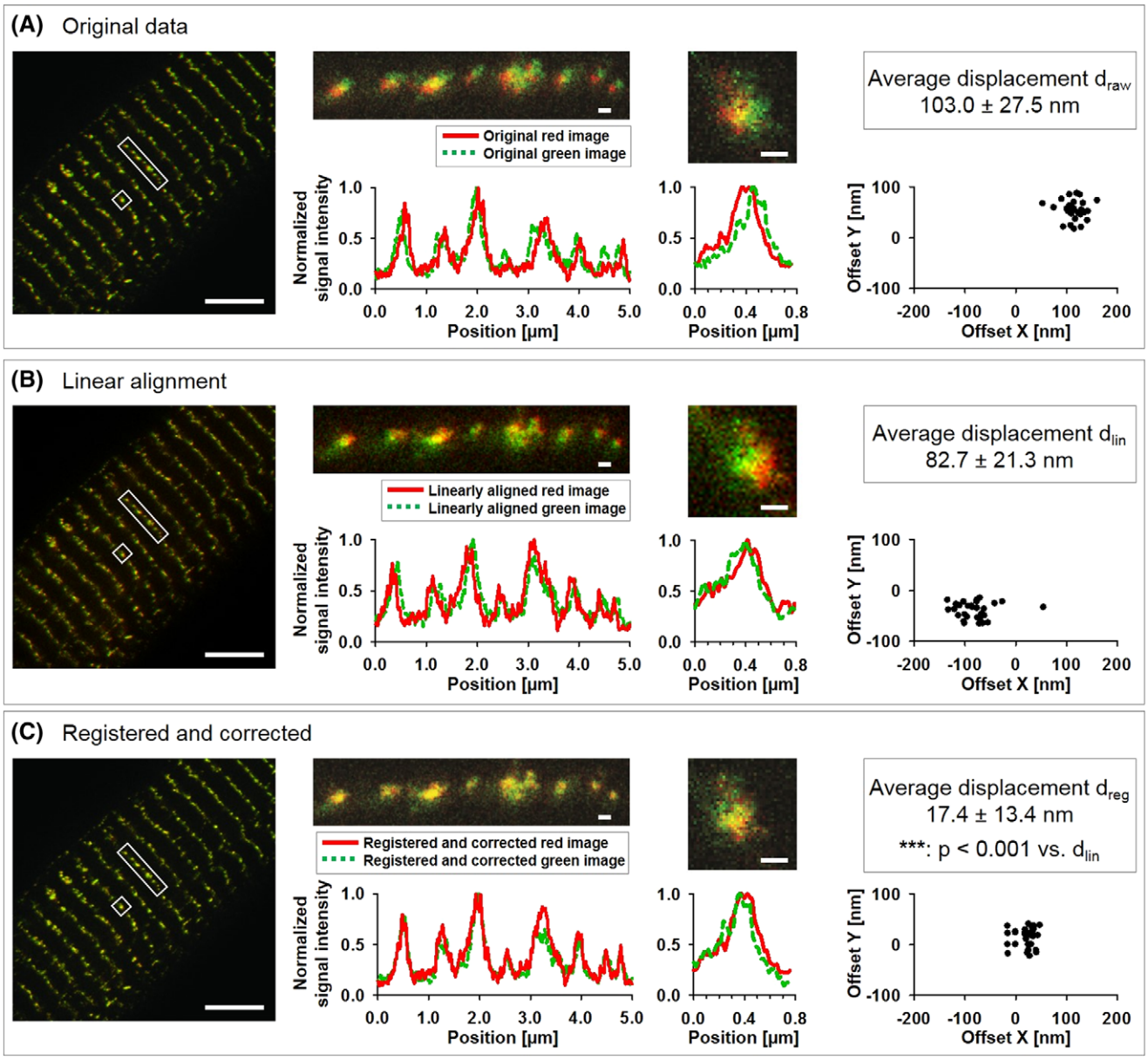

Fig. 4. Utility of the image registration protocol demonstrated by comparison of the original, linearly aligned, and corrected STED image data from a calibration sample of fixed murine cardiomyocytes in which the same protein – the ryanodine receptor type 2 (RyR2) – was labelled for both green and red colour channel detection (see *Immunofluorescence-labelling of cardiomyocytes* section). For the green colour channel, the fluorescent dye STAR488 (depicted in green in each image and in a green dashed line in each graph) and for the red colour channel, STAR635P (depicted in red in each image and in a red solid line in each graph) were used. (A)–(C) show corresponding images as follows: (A) original unprocessed STED image data, (B) linearly aligned STED image data and (C) the corrected and registered STED image data. Specifically, the images show the overlay of the green and red colour channel signals; yellow signals indicate substantial overlap between the green and red signals. The left panel in each (A), (B) and (C) displays a 20 × 20 µm² field of view for which two selected regions are magnified: a transversal arrangement of multiple RyR2 clusters (middle panel, corresponding to the rectangular boxed region) and a single RyR2 channel cluster (right panel, corresponding to the square boxed region). The apparent increase in yellow signal regions after image registration (i.e. A vs. C), indicates improved signal overlap, as expected for any two-colour immunofluorescence protocol using two antibodies against the same protein. However, linear alignment (see B) did not yield the same degree of signal overlap as the corrected and registered data (see C). Magnified image regions are accompanied by graphs of the normalised signal intensity as described in the main text. Here, the increased signal overlap is apparent and further quantified in the main text. Scatter plots display the distribution in colour channel offset each for the *X*- and *Y*-direction, determined as described in *Validation of image registration* section. Average signal peak distances are displayed as mean ± standard deviation. Using the two-sided Mann–Whitney–Wilcoxon U test (see *Validation of image registration*) the decrease of d_{reg} compared to d_{lin} was found to be statistically highly significant ($p < 0.001$, 150 data points each for d_{lin} and d_{reg}). Scale bars: 5 µm (overview images); 200 nm (magnifications).

transversal Z-line striation (corresponding to the rectangular boxed region) and a single signal spot originating from an individual dual-colour labelled RyR2 protein cluster (corresponding to the square boxed region). The two-colour channels are displayed in red and green in the overlay image; yellow signals indicate significant channel overlap. The magnifications of the respective overview images are accompanied by graphs, which illustrate the normalised signal intensity distributions with the red colour channel signal shown in red (solid lines) and the green colour channel signal shown in green (dashed lines). Two-dimensional scatter plots display the distributions of the colour channel offset in the *X*- and the *Y*-direction, determined as described in *Validation of image registration* section. As a result, the average displacement between the colour channels in nm is displayed as mean ± standard deviation.

Comparing the overlay images and the corresponding signal intensity distributions as displayed in Figures 4(A)–(C), it appears that the channel overlap gradually increases from the original data, through the linearly aligned data, and finally the fully corrected and registered data, that is, substantially more yellow signal indicates increased channel overlap between the signal peak intensity distributions. The scatter plots displaying the colour channel offset in the *X*- and *Y*-direction also reflect this increase of colour channel overlap. In detail, for the original data (Fig. 4A), the offset amounts to approximately 100 nm in both the *X*- and the *Y*-direction. For the linearly aligned data (Fig. 4B), both the offset in the *X*- and the *Y*-direction assume negative values. This might be due to a relatively large average shift vector ξ determined for the linear alignment procedure as described above. Because ξ was found to show a relatively high variance, the simpler linear alignment procedure seems to be insufficient for proper colour channel registration. In contrast, the registered and corrected image data by the registration protocol as proposed (Fig. 4C), markedly reduced the colour channel offset both in the *X*- and *Y*-direction and regularly resulted in values below the length of 1 px, that is, below 23.7 nm.

To quantify the improvement in colour channel overlap, the average displacement between the signal peaks of the same biological structure yet from two different colour channels was determined as described in *Validation of image registration* section. The displacement in nm is denoted in Figure 4 as mean ± standard deviation for the original data (d_{raw}), for the linearly aligned data (d_{lin}) and for the registered and corrected data (d_{reg}). Note that the values displayed for the displacement between the signal peaks was determined from a total of 5 cells from the cardiomyocyte calibration sample with 30 extracted peak signals per cell, whereas the displayed scatter plots show the colour channel offset for the image data of the specific cardiomyocyte shown in Figure 4. We found the average signal peak distance for the unprocessed data (d_{raw}) to be $d_{raw} = 4.55 \pm 1.21$ px, corresponding to 103 ± 27.5 nm. For the linearly aligned images, we obtained the signal peak distance $d_{lin} = 3.49 \pm 0.90$ px, corresponding to 82.7 ± 21.3 nm, providing only a minor improvement of $d_{raw} - d_{lin} \approx 20.3$ nm in colour channel overlap. In contrast, for the registered and corrected data, we obtained a signal peak distance $d_{reg} = 0.77 \pm 0.59$ px, corresponding to 17.4 ± 13.4 nm, which is well below the image pixel size of 22.7 nm. The decrease in signal peak distance d_{reg} as compared to d_{lin} was highly significant ($p = 3.7 \times e^{-11}$; sample size 150 data points for each d_{lin} and d_{reg}; two-sided Mann–Whitney–Wilcoxon U test; see also *Validation of image registration* section). This result confirms a significant improvement in signal structure overlap for the registered and corrected data, based on the registration protocol, as compared to the linear alignment procedure.

Thus, compared to the original data, image registration yields an overall improvement of signal overlap of $\Delta_d = d_{raw} - d_{reg} \approx 85.6$ nm, thereby validating the accuracy of the image registration protocol.

In summary, by obtaining the above described parameters $\delta\eta_1$, $\delta\eta_2$, and finally Δ_d, and by fulfilling the three described criteria, the two-colour image registration approach was quantitatively validated. Therefore, image registration can be used to improve the given STED image data and to confirm any subsequent quantitative image analysis based on routinely processed image data through the presented protocol and documentation steps.

Conclusions

We have developed a protocol to register and correct multicolour STED microscopy images based on imaging schemes that generally use more than one STED doughnut. Although the image registration protocol maximises the cross-correlation between defined image colour channels, it requires a relatively small number of images from a calibration sample in addition to the actual sample as data input. Henceforth, the image registration protocol consists of four major steps that we have thoroughly investigated and validated:

(1) Prior validation of the beam alignment status for any 'multi-doughnut' STED microscope configuration.
(2) A robust calibration sample is used for detailed documentation of the optimal image acquisition strategy.
(3) The image registration procedure systematically shifts the selected image channels against each other to achieve the maximal cross-correlation.
(4) Principle validation of the image registration protocol through specific criteria, which can be fulfilled and documented as milestone for further image analysis.

Finally, we have shown the principle applicability and validity of the image registration protocol for two-colour fluorescence labelled cardiomyocytes, a relatively thick and terminally differentiated cell type of high structural subcellular complexity. Although, for clarity, we restricted the protocol to

two colour channels, each coupled to a different STED doughnut, the protocol can be readily expanded to three or more colour channels and/or STED beams.

Taken together, the new STED image registration protocol provides a general scheme for optimal preparation of multicolour, multi-doughnut STED microscopy images and thus facilitates rational protocol-based approaches for quantifiable and reproducible image analysis.

Acknowledgements

We thank Jan Keller-Findeisen (Department of NanoBiophotonics, Max Planck Institute for Biophysical Chemistry, Göttingen, Germany) for excellent technical support with the development of the MATLAB script (Supplemental File S2) and numerical calculation of the focal intensity distributions; Tobias Kohl for helpful suggestions and critical comments (Department of Cardiology & Pulmonology, University Medical Center Göttingen, Germany); Stefan W. Hell for support and Jaydev Jethwa (both Department of NanoBiophotonics, Max Planck Institute for Biophysical Chemistry, Göttingen, Germany) for proof-reading.

Conflict of interest

The authors declare no conflict of interest for financial or any other reasons.

Funding sources

This study was supported by grants from the Deutsche Forschungsgemeinschaft (collaborative research center SFB 1002 subproject A09 and service project S02 to S.E.L.; SFB 1190 subproject P03); and by the German Center for Cardiovascular Research DZHK (UMG GOE MD3 to S.E.L.). S.E.L. is a principal investigator of the DZHK.

References

Berning, S., Willig, K.I., Steffens, H., Dibaj, P. & Hell, S.W. (2012) Nanoscopy in a living mouse brain. *Science* **335**, 551.

Bethge, P., Chereau, R., Avignone, E., Marsicano, G. & Nagerl, U.V. (2013) Two-photon excitation STED microscopy in two colors in acute brain slices. *Biophys. J.* **104**, 778–785.

Blom, H., Ronnlund, D., Scott, L., Spicarova, Z., Rantanen, V., Widengren, J., Aperia, A. & Brismar, H. (2012) Nearest neighbor analysis of dopamine D1 receptors and Na plus -K plus -ATPases in dendritic spines dissected by STED microscopy. *Microsc. Res. Techniq.* **75**, 220–228.

Brandenburg, S., Kohl, T., Williams, G.S. *et al.* (2016) Axial tubule junctions control rapid calcium signaling in atria. *J. Clin. Invest.* **126**, 3999–4015.

Buckers, J., Wildanger, D., Vicidomini, G., Kastrup, L. & Hell, S.W. (2011) Simultaneous multi-lifetime multi-color STED imaging for colocalization analyses. *Opt. Express* **19**, 3130–3143.

Chen, X.Z., Liu, Y.J., Yang, X.S., Wang, T.T., Alonas, E., Santangelo, P.J., Ren, Q.S. & Xi, P. (2013) Two-color CW STED nanoscopy. *Proc. SPIE.* **8590**, 859017-1–859017-7.

Chojnacki, J., Staudt, T., Glass, B. *et al.* (2012) Maturation-dependent HIV-1 surface protein redistribution revealed by fluorescence nanoscopy. *Science* **338**, 524–528.

D'Este, E., Kamin, D., Gottfert, F., El-Hady, A. & Hell, S.W. (2015) STED nanoscopy reveals the ubiquity of subcortical cytoskeleton periodicity in living neurons. *Cell Rep.* **10**, 1246–1251.

D'Este, E., Kamin, D., Velte, C., Gottfert, F., Simons, M. & Hell, S.W. (2016) Subcortical cytoskeleton periodicity throughout the nervous system. *Sci. Rep.-UK.* 6: **22741**, 1–8.

Danzl, J.G., Sidenstein, S.C., Gregor, C., Urban, N.T., Ilgen, P., Jakobs, S. & Hell, S.W. (2016) Coordinate-targeted fluorescence nanoscopy with multiple off states. *Nat. Photonics.* **10**, 122–128.

Donnert, G., Keller, J., Medda, R. *et al.* (2006) Macromolecular-scale resolution in biological fluorescence microscopy. *P. Natl. Acad. Sci. U.S.A.* **103**, 11440–11445.

Donnert, G., Keller, J., Wurm, C.A. *et al.* (2007) Two-color far-field fluorescence nanoscopy. *Biophys. J.* **92**, L67–L69.

Dunn, K.W., Kamocka, M.M. & McDonald, J.H. (2011) A practical guide to evaluating colocalization in biological microscopy. *Am. J. Physiol. Cell Physiol.* **300**, C723–C742.

Gottfert, F., Wurm, C.A., Mueller, V., Berning, S., Cordes, V.C., Honigmann, A. & Hell, S.W. (2013) Coaligned dual-channel STED nanoscopy and molecular diffusion analysis at 20 nm resolution. *Biophys. J.* **105**, L01–L03.

Hanne, J., Falk, H.J., Gorlitz, F., Hoyer, P., Engelhardt, J., Sahl, S.J. & Hell, S.W. (2015) STED nanoscopy with fluorescent quantum dots. *Nat Commun.* **6**, 7127.

Hell, S.W. (2007) Far-field optical nanoscopy. *Science* **316**, 1153–1158.

Hell, S.W. (2015) Nobel lecture: nanoscopy with freely propagating light. *Rev. Mod. Phys.* **87**, 1169–1181.

Hell, S.W. & Wichmann, J. (1994) Breaking the diffraction resolution limit by stimulated-emission-stimulated-emission-depletion fluorescence microscopy. *Opt. Lett.* **19**, 780–782.

Keller, J., Schonle, A. & Hell, S.W. (2007) Efficient fluorescence inhibition patterns for RESOLFT microscopy. *Opt. Express* **15**, 3361–3371.

Meyer, L., Wildanger, D., Medda, R., Punge, A., Rizzoli, S.O., Donnert, G. & Hell, S.W. (2008) Dual-color STED microscopy at 30-nm focal-plane resolution. *Small* **4**, 1095–1100.

Neumann, D., Buckers, J., Kastrup, L., Hell, S.W. & Jakobs, S. (2010) Two-color STED microscopy reveals different degrees of colocalization between hexokinase-I and the three human VDAC isoforms. *PMC Biophys.* **3:4**, 1–15.

Opazo, F., Punge, A., Buckers, J., Hoopmann, P., Kastrup, L., Hell, S.W. & Rizzoli, S.O. (2010) Limited intermixing of synaptic vesicle components upon vesicle recycling. *Traffic* **11**, 800–812.

Preibisch, S., Saalfeld, S., Schindelin, J. & Tomancak, P. (2010) Software for bead-based registration of selective plane illumination microscopy data. *Nat. Meth.* **7**, 418–419.

Reed, M.A., Randall, J.N., Aggarwal, R.J., Matyi, R.J., Moore, T.M. & Wetsel, A.E. (1988) Observation of discrete electronic states in a zero-dimensional semiconductor nanostructure. *Phys Rev Lett.* **60**, 535–537.

Wagner, E., Brandenburg, S., Kohl, T. & Lehnart, S.E. (2014) Analysis of tubular membrane networks in cardiac myocytes from atria and ventricles. *J. Vis. Exp.* **92**, 1–19.

Wagner, E., Lauterbach, M.A., Kohl, T. *et al.* (2012) Stimulated emission depletion live-cell super-resolution imaging shows proliferative

remodeling of T-tubule membrane structures after myocardial infarction. *Circ. Res.* **111**, 402–414.

Walling, M.A., Novak, J.A. & Shepard, J.R. (2009) Quantum dots for live cell and in vivo imaging. *Int J Mol Sci.* **10**, 441–491.

Wegner, K.D. & Hildebrandt, N. (2015) Quantum dots: bright and versatile in vitro and in vivo fluorescence imaging biosensors. *Chem Soc Rev.* **44**, 4792–4834.

Westin, L., Reuss, M., Lindskog, M., Aperia, A. & Brismar, H. (2014) Nanoscopic spine localization of Norbin, an mGluR5 accessory protein. *BMC Neurosci.* **15.1**, 45–53.

Zinchuk, V., Zinchuk, O. & Okada, T. (2007) Quantitative colocalization analysis of multicolor confocal immunofluorescence microscopy images: pushing pixels to explore biological phenomena. *Acta Histochem. Cytochem.* **40**, 101–111.

Supporting Information

Additional Supporting information may be found in the online version of this article at the publisher's website:

Supplementary Information.

